Co-variations of cerebral blood volume and single neurons discharge during resting state and visual cognitive tasks in non-human primates

Julien Claron, Matthieu Provansal, Quentin Salardaine, Pierre Tissier, Alexandre Dizeux, Thomas Deffieux, Serge Picaud, Mickael Tanter, Fabrice Arcizet, Pierre Pouget

Cell Reports

Article

Co-variations of cerebral blood volume and single neurons discharge during resting state and visual cognitive tasks in non-human primates

Graphical abstract

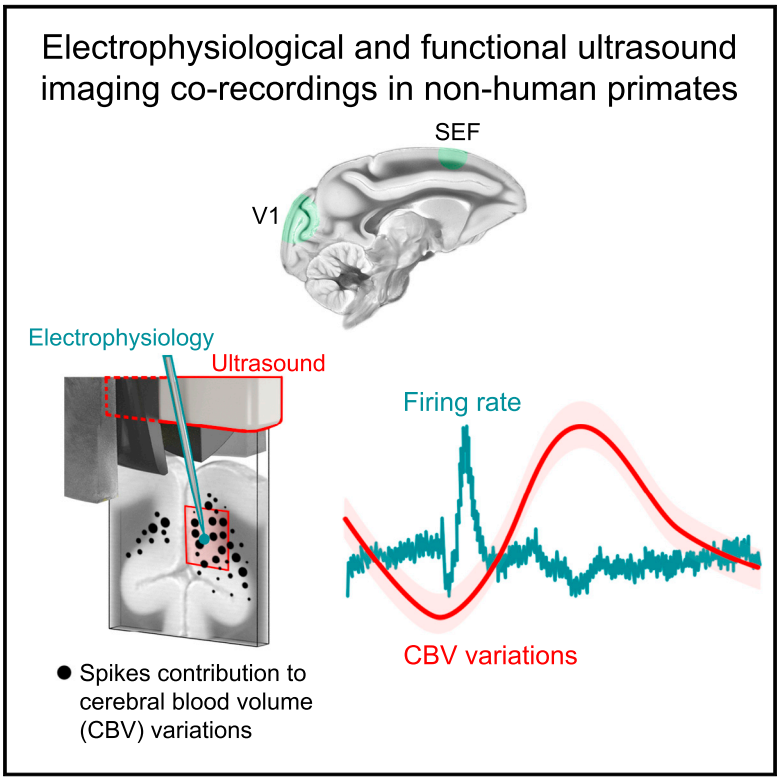

Highlights

- Co-recording of single-unit activity (SUA) and vascular activity in awake, behaving primates
- SUA provides a local contribution to cerebral blood volume (CBV) variations
- SUA and CBV are uncorrelated during resting state but correlate during behavioral tasks

Authors

Julien Claron, Matthieu Provansal, Quentin Salardaine, ..., Mickael Tanter, Fabrice Arcizet, Pierre Pouget

Correspondence

mickael.tanter@espci.fr (M.T.), fabrice.arcizet@inserm.fr (F.A.), pierre.pouget@icm-institute.org (P.P.)

In brief

Claron et al. achieve co-recording of single-unit activity (SUA) and functional ultrasound imaging in the brain of awake, behaving macaques. Their results show that SUA provides a local contribution to cerebral blood volume variations during tasks but not during resting state.

Claron et al., 2023, Cell Reports *42*, 112369
April 25, 2023
https://doi.org/10.1016/j.celrep.2023.112369

CellPress

Cell Reports

CellPress
OPEN ACCESS

Article

Co-variations of cerebral blood volume and single neurons discharge during resting state and visual cognitive tasks in non-human primates

Julien Claron,[1,3,5] Matthieu Provansal,[2,5] Quentin Salardaine,[3] Pierre Tissier,[3] Alexandre Dizeux,[4] Thomas Deffieux,[4] Serge Picaud,[2] Mickael Tanter,[4,*] Fabrice Arcizet,[2,*] and Pierre Pouget[3,6,*]

[1]Stem Cell and Brain Research Institute, INSERM U1208, Bron, France
[2]Institut de la Vision, CNRS, INSERM, Sorbonne Université, Paris, France
[3]Paris Brain Institute, Institut du Cerveau, INSERM 1127, CNRS 7225 Sorbonne Université, Paris, France
[4]Physics for Medicine, ESPCI, INSERM, CNRS, PSL Research University, Paris, France
[5]These authors contributed equally
[6]Lead contact
*Correspondence: mickael.tanter@espci.fr (M.T.), fabrice.arcizet@inserm.fr (F.A.), pierre.pouget@icm-institute.org (P.P.)
https://doi.org/10.1016/j.celrep.2023.112369

SUMMARY

To better understand how the brain allows primates to perform various sets of tasks, the ability to simultaneously record neural activity at multiple spatiotemporal scales is challenging but necessary. However, the contribution of single-unit activities (SUAs) to neurovascular activity remains to be fully understood. Here, we combine functional ultrasound imaging of cerebral blood volume (CBV) and SUA recordings in visual and fronto-medial cortices of behaving macaques. We show that SUA provides a significant estimate of the neurovascular response below the typical fMRI spatial resolution of 2mm^3. Furthermore, our results also show that SUAs and CBV activities are statistically uncorrelated during the resting state but correlate during tasks. These results have important implications for interpreting functional imaging findings while one constructs inferences of SUA during resting state or tasks.

INTRODUCTION

Awe-inspiring progress was enabled by novel technologies for imaging the entire brain at microscopic scale and at very high temporal resolution to study cortical thickness, microvascularization,[1,2] and neural or glial[3,4] functions in flies, fishes, and even rodents.[5–7] In large animals, the pioneering studies from Logothetis and colleagues showed that the impulse response of the neurovascular system weakly correlates with multi-unit activity, suggesting that the blood-oxygen-level-dependent (BOLD) signal does not predominantly reflect the output signal of neuronal processing.[8] Similarly, other studies found that BOLD fluctuations loosely relate to action potential frequencies in cats[9,10] and in non-human primates.[11,12] However, other studies have shown that the BOLD signal provided a reliable measure of firing rates in cats,[13] non-human primates,[14,15] and humans.[16] For example, a recent study showed that BOLD-derived population receptive fields (pRFs) were similar to multi-activity-related pRFs.[17] Others demonstrated that visual stimuli-induced early variations of oxygen are reliable estimates of spiking activity. Moreover, hemodynamic activity is also dependent on other non-neural fluctuations.[18] Finally, optogenetic driving of neuronal activity generates BOLD signals that correlate with firing rate in rodents.[19,20] This disparity of results can be resolved using an imaging technique with higher spatial resolution than fMRI to investigate the contribution of single-unit spiking to the neurovascular system.

Functional ultrasound imaging (fUS) is an innovative imaging technique that can provide whole-brain maps of neurovascular activity changes[21] even in deeper regions (up to 1.5 cm) with an approximately 5- to 10-fold better spatiotemporal resolution and sensitivity than fMRI (100 μm, 1 Hz, even if uniplanar fMRI sequences allow the same temporal resolution, the spatial resolution is unachieved with typical fMRI sequences). Like fMRI, the fUS technique relies on the neurovascular coupling of brain activity, but unlike BOLD signals, fUS measures changes in the cerebral blood volume (CBV) within microvessels using ultrafast Doppler[22] combined with spatiotemporal clutter filtering.[23] The fUS technique requires no large magnetic machinery and so has been applied in freely moving small animals using miniature, head-mountable transducers.[24] Several studies used fUS to investigate sensory processing in rodents[25–29] and in behaving primates.[30–32] Besides, an increasing number of studies have demonstrated that fUS can monitor brain activity in humans during surgeries[33] but also through the skull bone in neonates[29,34,35] or even adult patients.[36] Further knowledge of the contribution of neuronal activity to the CBV variations in humans and close species is therefore important for future interpretations of such basic and preclinical studies. To our knowledge, fUS and recording of nearby spiking activity has been achieved in rodents only.[37,38] However, the rodent model does not allow complex behavioral studies, and its brain architecture is quite far from that of humans, and therefore the non-human primate (NHP) model might

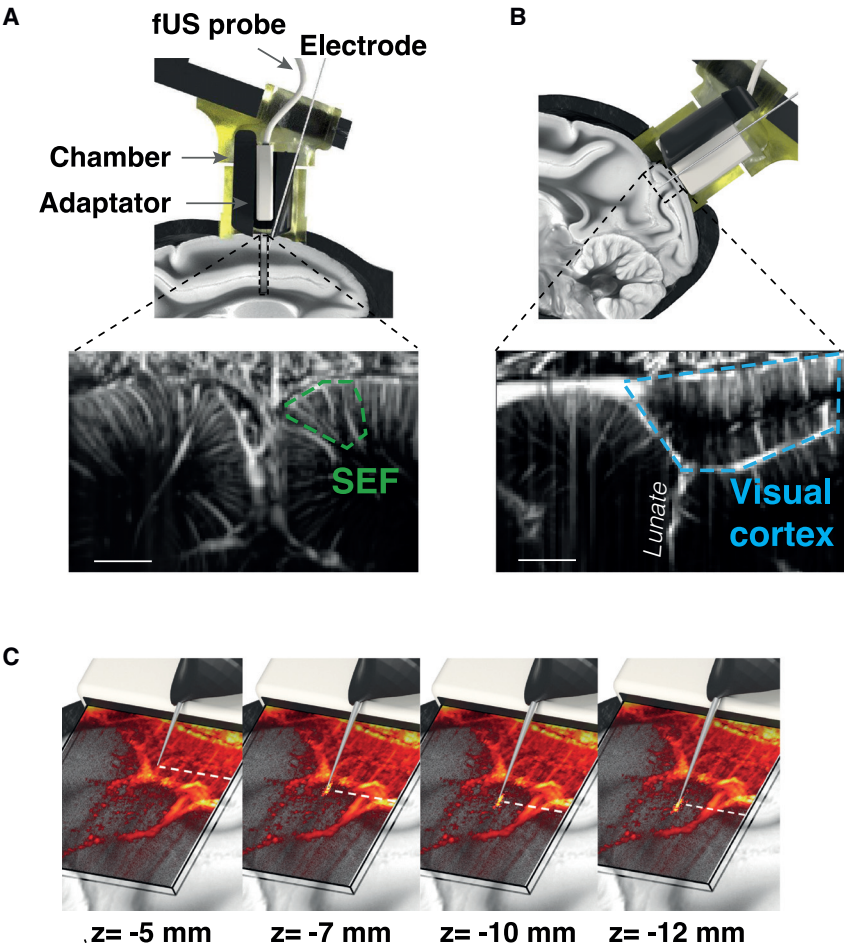

Figure 1. Experimental setup

(A) Co-localization adaptor. We used this setup on both animals; here, it is illustrated for the recording of SEF activities. Top panels: a custom cylindric adapter allowed the placement of a custom fUS probe (128 elements, 15 MHz, 100 × 100 μm^2 of spatial resolution) into the recording chamber. A micromanipulator was screwed on top of the adaptor and controlled the insertion of a single-channel electrode through the cortex via a tilted guide tube so that the tip of the electrode was placed in the fUS plane. Bottom: fUS of the SEF. Spatial scale bar: 2 mm.

(B) Co-recording adapter. We used this setup on both animals; here, it is illustrated for the recording of the visual cortex activities. Same as the co-localization adapter except the single-channel electrode is inserted parallel to the fUS plane. Spatial scale bar: 2 mm.

(C) Online tracking of microelectrodes. fUS of the region of interest (visual cortex here) was performed while inserting a single-channel electrode through the brain tissue. A high Power Doppler signal was detected when the tip of the electrode reached the fUS plane at z = 5 mm. This high Power Doppler signal extended downward when further inserting the microelectrode (z = 7, 10, and 12 mm, respectively).

allow to transpose the ins and outs more easily to the human brain. One recent publication concomitantly performed neural activity recordings and fUS for the first time in mice.[39] Their results show that CBV variations match the smoothed firing rates of nearby neurons, especially inhibitory, in the visual cortex and the hippocampus. A direct comparison between fUS signals and spiking activity has not been achieved in behaving primates. Furthermore, such comparison permits us to characterize a bit more the nature of resting state in primates, which has been extensively studied in humans[40,41] but rarely to a coupled neuronal/vascular point of view. Consequently, new protocols are needed to achieve simultaneous recordings of CBV and neural spiking in behaving primates. Most fUS studies have assessed the significance of CBV variations,[21,25,31] sometimes compared with spiking activity,[37] using covariate statistical analysis. To go a step further, we implemented from the fUS signal a generalized linear model (GLM) method estimate, allowing us to separate stimulus-induced, neural spiking, and noise signals. This approach facilitates a direct comparison of our results with those from fMRI studies.

In this article, we wanted to examine the contribution of single-unit activity to CBV variations. Using a protocol including ultrafast and high-resolution ultrasound imaging techniques (fUS) combined with commonly used electrophysiological systems in awake NHPs, we recorded both fUS and single-unit activities in the visual cortex and supplementary eye field (SEF) for monkeys L and S, respectively, while animals performed passive fixation and saccade tasks. We chose to focus on two different cortical areas to generalize the relationship between neural spiking and CBV variations. Our method permits online microelectrode position tracking and the recording of electrophysiological and CBV signals in awake, behaving animals. We computed stimuli-induced and spiking-induced activation maps using a GLM. Our results demonstrate that individual unit activities provide a significant estimate of the neurovascular system response.

RESULTS

Our first main result is that we could use our imaging method to perform precise online tracking and guidance of microelectrodes. The chambers were located above the SEF and the primary visual cortex (V1) for monkeys S and L, respectively (Figures 1A and 1B). The adaptor was designed and 3D printed to allow the technical challenge of co-recording nearby spiking signal and CBV variations of the imaging plane. By slowly inserting the microelectrode into the brain, we detected on the image a precisely localized high rise in the Power Doppler in the region of interest at z = 5 mm (Figure 1C), indicating that the tip of the electrode reached the imaging plane. When we inserted the electrode further, the high Power Doppler signal extended vertically downward, allowing us to detect the electrode progression through the thickness of the imaging plane from z = 5 to 12 mm (Figure 1C). In our study, we obtain an image every

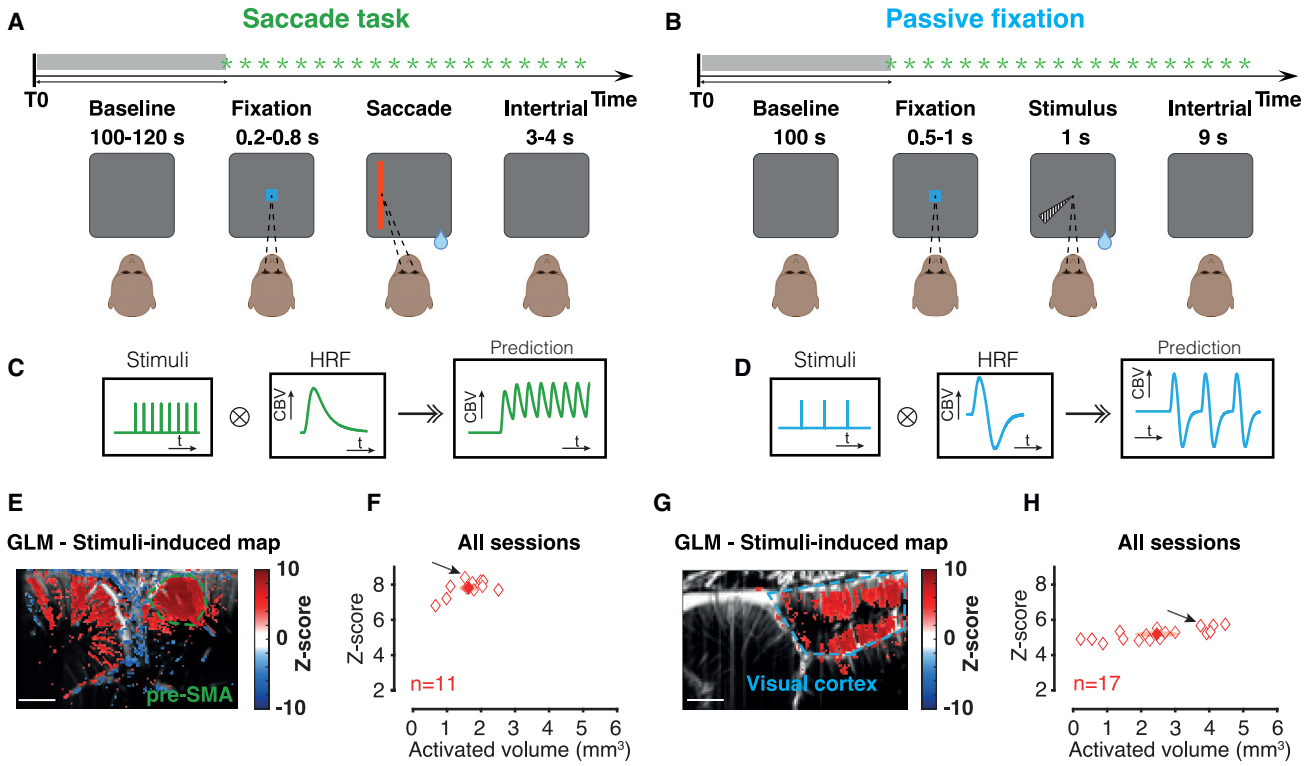

Figure 2. Task-related CBV responses

(A and B) Behavioral tasks. Both tasks began with a baseline period (no stimulus).

(A) Saccade task. Following an initial fixation of a central spot, the animal had to perform a saccade or anti-saccade task depending on the cue that appeared on screen (vertical or horizontal bar, respectively).

(B) Passive fixation task. Following an initial fixation of a central spot, the animal had to maintain its gaze during 1 s while a visual stimulus (see STAR Methods for the different stimuli) appeared on screen.

(C and D) Task-based generalized linear model (GLM). For each animal and cortical area (blue: SEF, green: visual cortex), we computed a behavior-based ΔCBV prediction by convoluting the stimulation pattern (timings of cue presentation) with the hemodynamic response function (HRF). Through t tests, we then obtained activation maps that represent the *Z* score for all voxels above a significance threshold ($p < 0.001$ after Benjamini-Hochberg correction).

(E and G) Representative activation maps of (E) the SEF and (G) the visual cortex. Colored dashed lines represent the regions of interest.

(F and H) Scatterplots of the median *Z* score of activation of each session against its volume for (F) the SEF and (H) the visual cortex. Plain symbols display mean data. Ellipses represent the SD in each dimension. Spatial scale bar: 2 mm.

0.4 s and a pixel resolution of 100 × 100 μm^2. To track the electrode, we need to see a difference of at least one pixel between images, so the minimum insertion speed is 100/0.4 = 250 μm/s. Indeed, we noticed a higher Power Doppler signal localized at the position of the tip of the electrode (Figure 1C) characterizing its motion during the insertion. Thus, our method permits precise online tracking of microelectrodes in the brain in awake, behaving primates.

Having established a method to place microelectrodes accurately in or near the fUS plane, we concomitantly recorded CBV and single-unit activity while the animals performed behavioral tasks. Monkey S performed a visual stimuli-guided pro-saccade or anti-saccade task with equal proportion for both conditions (Figure 2A; see STAR Methods). Monkey L performed a passive fixation task during which a peripheral visual stimulus was presented (Figure 2B). We used a repertoire of different visual stimuli (see STAR Methods) to generate different activation maps of the visual cortex. For most sessions, a single stimulus was presented. For others, hemi-concentric bands of varying eccentricities or squared-shape gratings with varying spatial frequencies were used (Figure S2). For monkey S, we recorded a total of n = 18 fUS sessions, and for monkey L, n = 79 fUS sessions (53 in which we also co-recorded single units). For the V1, we first built mean retinotopic maps on different imaging planes (Figure S1). The eccentricity selectivity our results show is in agreement with previous results.[31] Then, to test whether this spatial regionalization of the activation is accompanied by differences in CBV dynamics, we plotted the mean CBV variations of pixels sharing the same selectivity. Except for a significant difference of timing to reach the maximum between the 2° and 6° conditions and between the 6° and 14° conditions ($p = 0.0334$ and 0.0035, respectively, Kruskal-Wallis followed by multi-comparison test), we did not observe significant differences between maxima, minima, and the minima timings ($p = 0.8419$, 0.3211, and 0.6283, respectively, Kruskal-Wallis). Therefore, we generated a single hemodynamic response function (HRF) by averaging the mean CBV response over sessions and computing the gamma inverse function that fit best. Hence, we computed

the activation map induced by all stimuli presentations (independently from their nature) using the GLM approach. We add in Figure S2C another similar HRF of the SEF obtained in another animal. We also used the HRF from monkey L to simulate CBV variations using a protocol described by Blaize and colleagues and compared the results with the CBV variations published in this study from another monkey implanted over the V1 (Figure S2D). We found that our simulated results share the same profile as the data previously published. Furthermore, we obtained a maximum that is reached 2 s after the stimulus presentation, too. However, the simulation curve is shifted downward compared with the results from Blaize and colleagues.[31] This suggests that the HRF from this other animal might have an HRF with an undershoot that is relatively smaller compared with the positive phase than what we observed for monkey L in our study. For further analyses about the dynamic of activation between pro- and anti-saccades, see previous studies of Claron and colleagues.[42] In our model, we took as input the spatiotemporal Doppler images and took a stimuli-induced regressor (Figures 2C and 2D). Briefly, for each pixel, all visual stimulus presentation timings were convolved with the fUS-determined HRF of the investigated cortical area to obtain a CBV signal prediction. From the fit between these signal predictions and the real CBV variations, the *Z* scores and p value maps were obtained (Figures 2E for SEF and 2G for V1).

The activation maps show the *Z* score of all pixels in the images with a p value <0.001 (after Benjamini-Hochberg correction to decrease false discovery rate). Figure 2E shows a representative activation map induced by the presentation of both pro-saccade and anti-saccade stimuli for correct trials for monkey S (see STAR Methods for GLM application). We detected significant pixels in both hemispheres, although the right SEF (dashed green line) displayed more significant pixels, corresponding to an activated volume around 2 mm^3. All sessions were balanced in terms of ratio pro- vs. anti-saccades and left vs. right. Figure 2F represents the population analysis of median *Z* scores and volumes of activation in SEF for sessions in which activation was detected in the region of interest (n = 11). The mean stimuli-induced volume of activation in the SEF was 1.64 ± 0.54 mm^3 Figure 2G shows a representative activation map in the visual cortex induced by the stimulus presentation for correct trials for monkey L. We detected significant pixels in the superficial and deeper layers of the region of interest (V1 and V2, respectively) corresponding to an activated volume of 3.7 mm^3 Figure 2H represents the population analysis of median *Z* scores and volumes of activation in the visual cortex for sessions in which activation was detected in the region of interest (n = 17). The mean stimuli-induced volume of activation was 2.5 ± 0.7 mm^3.

For monkey S, among n = 18 imaging sessions, we recorded n = 18 single units. Among this pool of 18 neurons, we obtained n = 9 single units displaying a significant response locked to the saccade execution. For monkey L, among n = 53 imaging sessions, we recorded n = 17 single units displaying a significant response locked to the stimulus presentation. We then investigated the neurovascular response associated with isolated single-unit activities. To visualize the dynamics of the CBV responses, we plotted the averaged variation of CBV over time for all correct trials and for all pixels of each region of interest (delimitated by dotted lines in Figure 2). The SEF CBV variation rose after a dip synchronized with the stimulus presentation (t = 0 s) and reached a plateau around 3% 1.8 s later, before decreasing back to its initial value after 4 s (Figure 3A, bottom panel, red curve). The initial decrease in CBV preceding stimulus presentation reflects the end of the previous trial response, as trials are spaced with a 3–4 s inter-trial period. Figure S4 shows the same response profile for a session in which we performed fUS only and during which trials were spaced with 10 s; these results show that the previously mentioned decrease preceding stimulus presentation indeed reflects the tail of the previous trial response and does not seem due to stimulus prediction or variations in arousal as others have reported.[15,43,44] Here, during the same example session, we recorded the activity from a single unit located in the right SEF. The raster plot (Figure 3A, top panel) and the spike density function (Figure 3A, bottom panel, blue curve) show a transient increase of the firing rate (up to 30 Hz) that corresponds to the saccade execution, followed by a less active period. Note the different kinetics between the fast neuronal activation and the slower neurovascular response; the peak of the CBV response occurred 1.6 s after the firing rate peak.

We next wanted to test whether the spiking activity recorded with the single electrode at a close location could contribute to the neurovascular response. To do so, we used another GLM approach based on the spike's activity. Here, we convoluted for each animal the single-unit spike onsets with the HRF extracted from the same region of interest (Figures 3C for SEF and 3D for V1) to obtain a CBV signal prediction. As previously, the representative co-activation maps show the *Z* score of all pixels in the images with a p value <0.001 (before Benjamini-Hochberg procedure to decrease false discovery rate) obtained from the fit between the predicted signal and the real CBV variations (Figure 3E). We also represented the task-related activities displayed in Figure 2E for comparison (green transparent colored pixels). For monkey S, the co-activation map showed a spike-correlated neurovascular response in the SEF corresponding to a volume of ∼1.1 mm^3 (Figure 3G, left panel) compared with 2 mm^3 with the GLM based on stimuli. Interestingly, the spread of this co-activation was more localized than the activation detected with the GLM approach based on the stimulation pattern. Furthermore, the spread of this correlated activation was constrained around the electrode recording site (indicated by the dashed white line). We repeated these analyses for the visual cortex that revealed a different pattern of CBV variation. Indeed, the CBV variation displayed a biphasic increase up to 1.3% (Figure 3B, bottom panel, red curve). Interestingly, we detected a large undershoot in the visual cortex neurovascular response (from 4 to 8 s) before the signal went back to its initial value. This undershoot was absent from the SEF response. The raster plot (Figure 3B, top panel) and the spike density function (Figure 3B, bottom panel, blue curve) of simultaneous single-unit recordings show a transient increase of the firing rate (up to 11.5 Hz). Here, the neuronal activation was also faster than the neurovascular response with a difference of 2.45 s. We reported consistent results for monkey L (Figure 3G, right panel). As for monkey S, the spread of the spike-correlated activity was smaller (∼0.6 mm^3; Figure 3H) than the activation induced

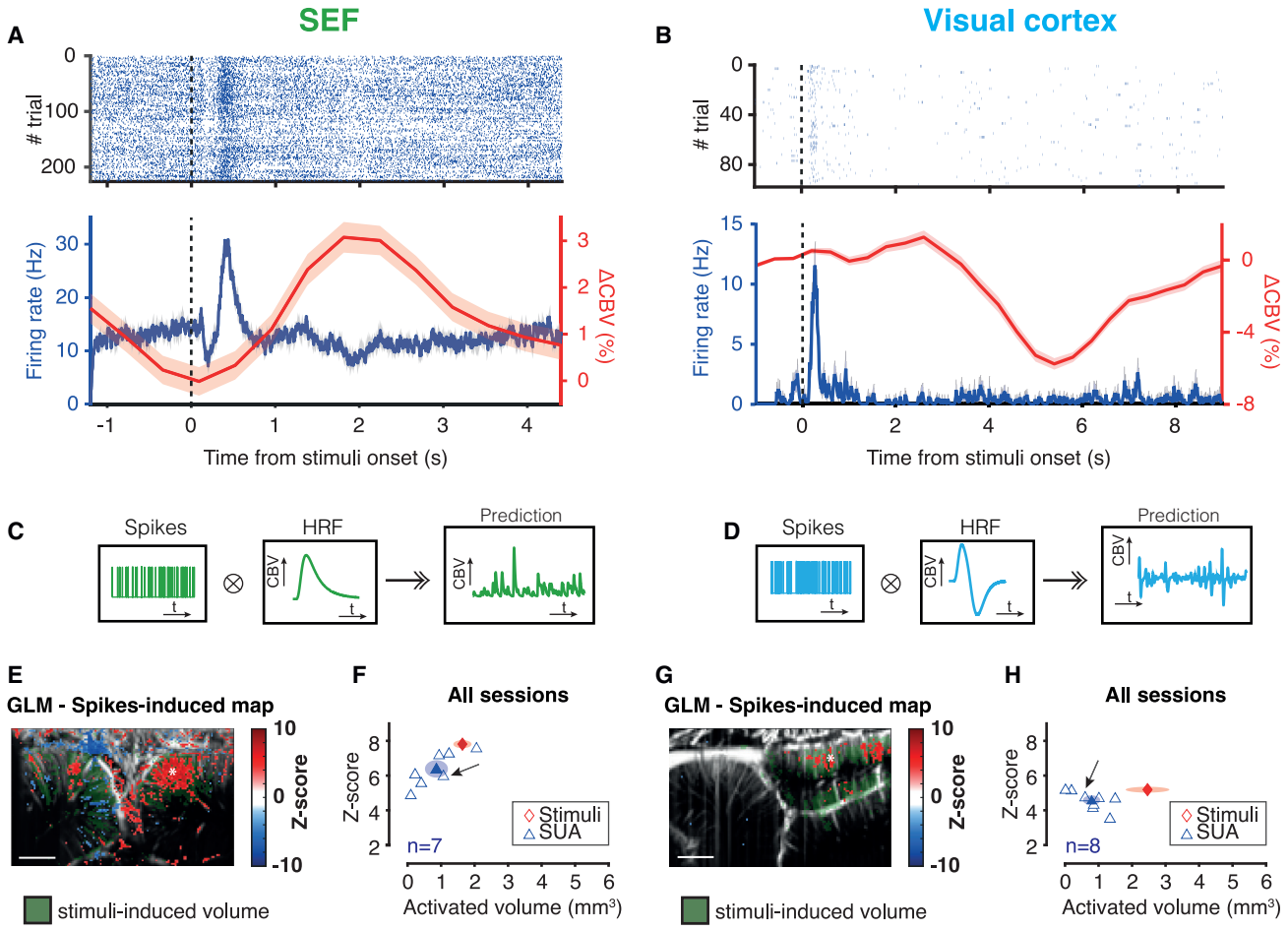

Figure 3. Spike's contribution to the CBV response

(A) Top: raster plot of the SEF single unit that was co-recorded with fUS, for correct trials only. Bottom: spike density function (SDF; blue curve) of the same single unit as above and ΔCBV from the region of interest (ROI) delimited in the SEF map in (E).

(B) Same but for the visual cortex activities extracted from the same example session than the visual cortex activation map in (G). t = 0 refers to the cue presentation. Data presented are mean ± SEM.

(C and D) GLM based on spike activities. Diagrams in each panel: same as Figures 2C and 2D, but the stimulus pattern is replaced by the spike's onset.

(E and G) Representative spike-induced activation maps of the SEF and the visual cortex, respectively. Colored dashed lines represent the ROIs. Stars represent the electrode insertion axis (distance circa 1 mm tangent to the imaging plane). Green-colored pixels represent the behavior-induced CBV response (shown in Figures 2E and 2G), which is more spread.

(F and H) Scatterplots of the median *Z* score of activation of each session against its volume for (F) the SEF and (H) the visual cortex. Task-induced and SUA-induced activations are represented by blue diamonds and red triangles, respectively. Task-induced volumes are more spread than SUA-induced volumes (F: p = 0.016, Student;'s t test; H: p = 1.3915e^{-4}, two-sample t test), and median *Z* score of stimuli-induced activation was higher than for SUA-induced activation (F: p = 0.0084, Student's t test; H: p = 0.0024, two-sample t test). Plain symbols display mean data. Ellipses represent the SD in each dimension. Spatial scale bar: 2 mm.

by stimuli onsets but was not particularly restricted around the electrode recording site. Furthermore, we run the same analyses on non-significant units (n = 2 for monkey S and n = 11 for monkey L). We found no contribution of spiking activity to the CBV activation in monkey S (Figure S6), but 9 units from monkey L displayed some contribution to the global neurovascular activity. This suggests that some of the CBV variations recorded during tasks can be explained by spontaneous activity of non-responding cells. Finally, we tested if the center of mass of the single-unit activity (SUA)-related activity correlated with the position of the recording site. For monkey L, we did not see any particular correlation between z coordinates (Figure S7), suggesting that the computed co-activity extends to distant pixels as shown in the example map. To conclude, these results demonstrate that our method allows examining specific links between SUAs and CBV variations in behaving NHPs.

To assess that the single-unit-induced activation is more localized than the stimuli-induced activation, we computed the volumes and median *Z* scores of activations for each condition over our entire pool of data (Figures 2F and 3F for SEF and 2H and 3H for V1). For monkey S, we showed that the mean stimuli-induced volume of activation in the SEF is 1.64 ± 0.54 mm^3,

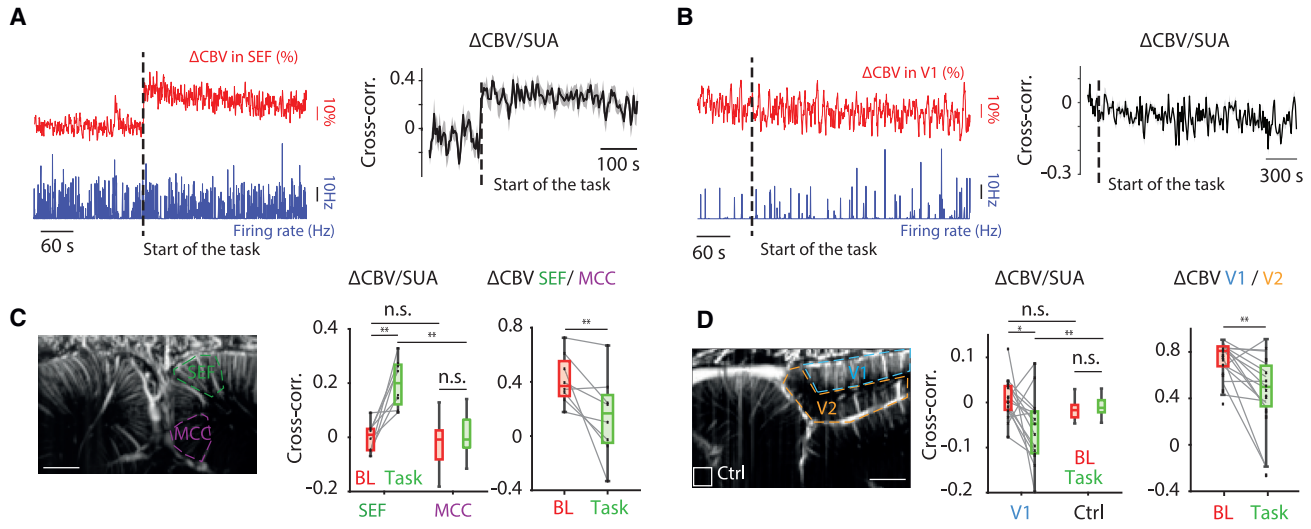

Figure 4. Intra- and inter-areas cross-correlation of neural spiking and CBV variations shift when behavioral task is engaged

(A) Left panel: example of CBV variations (red curve) and SDF (blue curve) during session for SEF. Right panel: mean sliding cross-correlation between CBV variations and SDF in SEF across all sessions (n = 9). Gray shaded area represents s.e.m.

(B) Same as (A) for V1 (n = 15 sessions).

(C) Left graph: mean cross-correlation between CBV variations and SDF during resting state (i.e., initial baseline [BL] of the recording session) and task for SEF and median cingulate cortex (MCC) (SEF BL/task, p = 2.6e−3; SEF task/MCC task, p = 1.2e−3, paired t test). Right graph: cross-correlation between CBV variations of SEF and MCC during resting state and task (p = 0.03 compared with resting state, paired t test). Error bars represent the minimum and maximum values, boxes the 1st and 3rd quartiles. Map: locations of the areas used before.

(D) Same as (C) for V1 and V2. Control area is a 1 × 1 mm^2 ROI located at the bottom left corner of fUS images for monkey L. Left panel: V1 BL/task, p = 0.0204; V1 task/control task, p = 0.0107, paired t test. Right panel: p = 0.0038, paired t test. Spatial scale bar: 2 mm.

whereas the SUA-induced volume of activation is 0.86 ± 0.68 mm^3 (Student's t test between the stimuli-induced- and the SUA-induced activities gives the former significantly higher than the latter, with p = 0.016, t test is chosen as data are Gaussian [Shapiro-Wilk test, p = 0.82 and 0.58 respectively] and F test gives similar variances [p = 0.49]). Peak *Z* score of GLM-calculated maps was found to be slightly higher for the stimuli-induced map (7.81 ± 0.47) than the *Z* score for the spikes map (6.39 ± 1.00; p = 0.0084, Shapiro-Wilk test assures that both *Z* scores for stimuli induced and SUA induced are Gaussian, F test assures that variances are unequal). We confirmed these results in the second animal: for monkey L, the mean stimuli-induced volume of activation of the visual cortex was significantly higher than the SUA-induced volume of activation (stimuli induced: 2.5 ± 0.7 mm^3, n = 17 acquisitions; SUA: 0.8 ± 0.5 mm^3, n = 8 responsive units, p = 1.3915e-4 two-sample t test with unequal variances as samples are Gaussian according to Shapiro-Wilk test [p = 0.6064 and 0.8096 for stimuli induced and SUA induced, respectively) as illustrated in Figure 3G for the example session. Interestingly, the median *Z* score of stimuli-induced activation was also significantly higher than the median *Z* score of SUA-induced activation (stimuli induced: 5.19 ± 0.17, n = 17 acquisitions; SUA: 4.58 ± 0.55 mm^3, n = 8 responsive units, p = 0.0024, two-sample t test as samples are Gaussian according to Shapiro-Wilk test [p = 0.2882 and 0.4771 for stimuli induced and SUA induced, respectively] and have equal variances according to F test [p = 0.0947]). Altogether, these results demonstrate that SUAs partially contribute to the cerebral blood flow variations in behaving NHPs.

With GLM analyses, we spatially characterized the relationship between neural spiking and CBV in two different cortical areas during behavioral tasks. One could also ask how both CBV and neural spiking are temporally linked. We next investigated how neural spiking contribution to the neurovascular activity changes between resting state (i.e., BL [baseline], 100 to 120 s long period before task onset) and the start of the task for responsive units. We first represented display examples of CBV variations and spike density function (SDF) over one unique session for the SEF and V1, respectively (Figures 4A and 4B). Results show a stark rise in CBV variations for the SEF when the task starts, unlike for the V1. This effect could be due to differences of physiology between these two areas. However, another explanation could be that the rise of CBV shown for the SEF is due to task-related changes of arousal since monkey S performs a more active task than fixation. Previous works[15,43,44] have indeed shown that variations in arousal can cause hemodynamic changes. Another hypothesis might be the shape of the HRF. The SEF HRF shape induces a buildup of the ΔCBV in the SEF, whereas the V1 HRF shape does not induce a buildup with our paradigm of stimulation. However, those two hypotheses are not mutually exclusive. We computed the moving non-overlapping cross-correlation across resting state and task between the fUS signal in the region of interest (ROI) and the SDF of the recorded single unit. We took into account the delay for which the absolute value of correlation or anti-correlation between those two signals was maximal: +2 s (SEF) and +5.2 s (V1) (Figures 4C and 4D, left graphs represent the mean and SEM of these moving cross-correlations across sessions for the SEF

[n = 9] and V1 [n = 15, two sessions missing initial BL]), respectively). We quantified the average values of cross-correlation during resting state and task for SEF and V1 and for two control areas: median cingulate cortex (MCC) for monkey S and a 1 × 1 mm^2 ROI located at the bottom left corner of fUS images for monkey L (see the locations of these areas in the maps of Figures 4C and 4D). Interestingly, both in the SEF and in the V1, there is no correlation between SDF and fUS signal during resting state (t test comparison with null distribution, SEF: p = 0.96, V1: p = 0.56), but these signals became correlated in the SEF and anti-correlated in the V1, respectively, after the task began (SEF r = 0.2 ± 0.03 SEM, p = 2.6e−3, V1 r = −0.06 ± 0.0096 SEM, p = 0.0204, t test). The anti-correlation in the V1 might be due to the undershoot of the HRF in this cortical area. Finally, we computed the correlation between CBV variations of different areas of the brain, both during resting state and during task, in order to characterize the vascular component of the default mode network and the variation due to the beginning of a behavioral task. In the median wall of primate brain, we observe a correlation between the SEF and the MCC during resting state (Figure 4C, right panel; r = 0.42 ± 0.07 SEM, p = 3.4e−4 t test comparison with null distribution) and a decrease of this correlation between the SEF and the MCC during the task (r = 0.15 ± 0.11 SEM, p = 0.20 compared with null distribution, p = 0.03 compared with resting state, t test), suggesting a vascular component of the default mode network and an alteration of vascular co-oscillations during active behavior, whereas neuron spiking and vascular activities synchronize during behavioral tasks. Similarly, in the visual cortex, the correlation between the V1 and the V2 during the BL is higher during the resting state (Figure 4D, right panel; r = 0.66 ± 0.019, p = 5.0e−11 compared with null distribution) than it is during task (r = 0.39 ± 0.083, p = 3.66e−4 compared with null distribution, p = 0.0038 compared with resting state, t test).

DISCUSSION

We have developed a methodology and associated setup to record simultaneous CBV and electrophysiological signals in awake, behaving macaques. Our method offers first to report online tracking of the microelectrode localization in the brain of behaving NHPs. The spatial resolution of ultrasound imaging offers an unprecedented ability to co-register microelectrode and microsensor and potentially any rigid pipettes around 100 μm wide within the ultrasound imaging referential frame. Further studies might combine our method to localize viral injections' pipette and may help quantify the spread of compound perfusion by mixing it with contrast agents such as SonoVue during surgeries with a deeper field of view than is allowed by optical imaging,[45] possibly allowing injections in subcortical areas. Functionally, fUS and electrophysiology do not seem to interfere with one another, or at least we were not able to measure the interference between them both, thus the coupling of the techniques is far easier than fMRI, optical imaging, and electrophysiology in awake, behaving primates. Previous studies have found that fUS could be combined with acute or chronic electroencephalogram (EEG) recordings in awake rodents[46,47] and multi- or single-unit recordings in anesthetized or awake rodents.[37,38] These pioneering studies in awake rodents have shown a marked change of fUS activity at the initiation of tasks but were limited to explore sensory or cognitive functions in deep cortical folded brain areas. Our study demonstrates that our methodology allows using standard protocols to record simultaneous CBV and electrophysiological signals in awake, behaving macaques without movements or electromagnetic artifacts. For the statistical assessment of CBV, some of these fUS studies used correlation methods of time-evoked variations of CBVs compared with the more standard protocols used in other imaging techniques such as fMRI. In this study, we report fUS analysis based on GLM standard statistical assessment in NHPs.[48] It depicts for each voxel its CBV variaions as the linear combination of the HRF with a regressor of interest (e.g., oculomotor or visual tasks) including spiking activity of our awake, behaving primates. This analysis proved the high sensitivity of our recording method and showed that brain activity could be investigated with minimal adaptation for different brain areas or electrophysiological systems (SEF and V1) in awake, behaving primates. We hypothesized that single-unit-induced activation is more localized than the stimuli-induced activation based on the significantly activated area estimated from the thresholded *Z* score maps. This assumes that there is no large difference in the statistics between both maps so that thresholding does not artificially reduce the activated area size. This seems to be generally the case, as both maps are constructed from the same acquisitions and parameters.

The relationship between both vascular and neuronal signals is still debated. Recent studies report striking inconsistencies between the fMRI and electrophysiological signals.[49] Previous fMRI studies have shown that the neurovascular activity (BOLD signal) provided a reliable measure of multi-unit activities.[13–15] Conversely, other studies have reported a poor correlation between multi-unit activities and the BOLD signal.[9,11,12] Others have furthermore demonstrated that non-neuronal factors such as variations of arousal[15,43,44] can influence the neuronal response. Our group has also demonstrated in previous studies[42] that CBV variations are correlated with variations of pupil diameter. Importantly, we demonstrated here that the cortical volume in which SUAs correlate significantly with CBV variations is smaller than the cortical volume in which task events correlate with cue presentation timings. Indeed, few works have spatially characterized spikes' contribution to the neurovascular system. It has been shown that blood flow variations in the olfactory bulb of rodents show a similar linear relationship with locally measured neuronal Ca^{2+}.[26] A recent publication showed that neural signals from the visual cortex and hippocampus in mice, and more particularly firing rates from inhibitory neurons, also correlate with fUS signals in mice. Co-activation maps from an fMRI study carried out in human subjects[16] have shown that SUA correlation with BOLD signal in Heschl's gyrus is more localized than the activity predicted by local field potential (LFP), although this result was more qualitative than quantitative. However, the authors tested the correlations between SUAs recorded in a first group of patients and the BOLD signals from other patients, whereas we perform here an intra-individual analysis. At least four hypotheses have been discussed that can explain the discrepancies between the two LFP and SUA

methods: (1) the BOLD signal follows LFP signals closer than spikes[8]; (2) the BOLD signal is reflecting electrophysiological signals that are occurring later due to feedback delay[50]; (3) the BOLD signal is more sensitive than traditional electrophysiological methods due to massive pooling by the hemodynamic coupling process[51]; and finally, (4) there are no real inconsistencies, and instead, small but reliable effects on firing rates may be obscured by differences in experimental design and interpretation of results across methods and statistical analysis.[52] Our main result demonstrates that a fifth explanation prevails. Indeed, fUS enables us to show that the cortical volume in which SUA correlates significantly with CBV variations is smaller than the cortical volume in which task events correlate with cue presentation timings. We demonstrated this in two behaving NHPs' primary visual and fronto-medial cortices. It consequently indicates that SUAs correlate with CBV variations recorded if and only if the blood dependent signal is extracted at sufficiently high spatiotemporal resolutions. As this is the case in fUS, we showed that SUAs provide a significant estimate of the neurovascular response with an activated area smaller than usual fMRI spatial resolution. Thereby, fUS seems to be the technique of choice in order to study neurovascular coupling in the brain of awake, behaving primates because of a higher spatial resolution (~200 μm). Another reason is that fUS is easier to interpret than fMRI, as CBV variations reflect only the supply of neurovascular units instead of the balance between the supply and demand that drives the BOLD signal.

fUS in awake, behaving NHPs allowed us also to study the difference of neurovascular responses between resting state and task. Resting state is believed to be the reflection of brain activity during rest,[53] but it is still unclear if this vascular activity, measured with fMRI, is the reflection of the neuronal activity, even though some studies use fMRI combined with EEG or magnetoencephalography (MEG) to assess the link between them both.[40,54–56] We demonstrated in this study that CBV and SUAs are uncorrelated during resting state and become correlated during various tasks. However, other studies have found that multi-unit activities sampled in larger volumes can predict spontaneous neural activity.[39,57] Furthermore, we found that CBV activities across known connected brain areas are correlated but decorrelate at the onset of the tasks as expected if participating in the default mode network (DMN). Additionally, resting-state fMRI or resting-state fUS is linked to neuronal activities during rest, as on-task fMRI/fUS are linked to neuronal activities during tasks, so the on-task decorrelation might reflect a change in local information in cortical area by suppressing the spontaneous neuronal activity from resting-state to task-oriented neuronal activity.[58] Therefore, BOLD measured in fMRI, as well as CBV measured with fUS, during resting state might not much reflect the neuronal activity but basal metabolic changes through glia and astrocytes or intrinsic connectivity through slow synchronized neuronal oscillations across distant brain areas.

With the current 2D visualization, displacement of the probe is required to map a large volumetric area. The 2D view remains one intrinsic limitation of our method to investigate the 3D brain activity. However, ongoing development to perform direct 3D ultrasound imagery with microprobes would certainly offer new options soon, as is already done in rodents using 3D array probes[59] or row-column addressed probes.[60] Finally, the use of multi-contact electrodes possibly introduced over an entire cortical region will allow the study of the dynamics and propagation of the relationship between electrophysiological signals and the vascular response. Within various parts of cortical areas of primates, the use of such a technique could undoubtedly allow the study of electrophysiological and vascular responses in layers and thus succeed in studying neurovascular coupling in primates at a spatial and temporal resolution never achieved.

Limitations of the study

This study established the relationship between neural spiking and CBV variations from n = 2 NHPs. Data from each subject were measured in different cortical areas (SEF and V1) and in the context of different behavioral tasks. Though we found in both animals/tasks that the volume in which SUA correlates significantly with CBV variations is smaller than the cortical volume that correlates with stimuli timings, our study also shows a difference in HRF between the two animals. One point that needs to be clarified is whether this disparity in HRF is due to physiological differences between SEF and V1 or inter-individual differences. Though we provide another example of SEF HRF from another animal (Figure S4) that matches the SEF HRF of the first animal, we do not provide confirmation of another V1 HRF displaying such undershoot.

Furthermore, when temporally describing the SUA/CBV relationship, we show in both monkeys that there is a shift in the sliding cross-correlation of these two parameters when the task begins. However, this shift happens faster in the SEF. Here too, more than our dataset is needed to conclude whether this observation is due to differences between cortical areas and tasks. Finally, more than our measurements are needed to spatially characterize the relationship between LFP and CBV variations. As LFP reports neuronal activity on a larger volume than SUA, one might anticipate that the cortical volume in which LFP correlates with CBV variations is more significant than the volume displaying CBV variations and SUA co-activity.

STAR★METHODS

Detailed methods are provided in the online version of this paper and include the following:

- KEY RESOURCES TABLE
- RESOURCE AVAILABILITY
  - Lead contact
  - Materials availability
  - Data and code availability
- EXPERIMENTAL MODEL AND SUBJECT DETAILS
- METHOD DETAILS
  - Behavioral training
  - Behavioral paradigm for SEF data
  - Behavioral paradigm for V1 data
  - Implant and probe for functional ultrasound imaging for awake Cooperative monkeys
  - Functional ultrasound (fUS) recordings
  - Eye movements and pupil recordings

- Online microelectrode position monitoring
- Definition and conduct of a recording session
- Extracellular electrophysiological recordings
- Setup preparation
- fUS data processing
- Retinotopic maps
- Processing of electrophysiological signals
- Cross-correlation between signals

● QUANTIFICATION AND STATISTICAL ANALYSIS

SUPPLEMENTAL INFORMATION

Supplemental information can be found online at https://doi.org/10.1016/j.celrep.2023.112369.

ACKNOWLEDGMENTS

Part of this work was carried out at the Phenoparc core facility of ICM. We gratefully ankowledge Morgane Weissenburger and Estelle Chavret-Reculon for day-to-day management of the animal facility and Bénédicte Daboval and Lucile Aubrée for veterinary care. This work was supported by the BrainOptoSight Agence Nationale de la Recherche (ANR) grant (AAPG2020 BrainOptoSight), by the Fondation pour la Recherche Médicale (FRM Equipe EQU202106012159 et FDT202106013150), and by French state funds managed by the ANR within Program Investissements d'Avenir, Laboratoire d'Excellence (LABEX) LIFESENSES (ANR-10-LABX-0065), and Institut Hospitalo-Universitaire FOReSIGHT (ANR-18-IAHU-0001).

AUTHOR CONTRIBUTIONS

Conceptualization, P.P., J.C., F.A., and M.T.; investigation, J.C., M.P., and Q.S.; writing – original draft, review & editing, J.C., M.P., T.D., F.A., P.P., and M.T.; visualization, J.C., M.P., A.D., F.A., and P.P.; funding, M.T., P.P., and S.P.; resources, P.T., P.P., M.T., and T.D.; supervision: F.A., P.P., M.T., and S.P.

DECLARATION OF INTERESTS

M.T. and T.D. are co-inventors of several patents in the field of functional ultrasound neuroimaging and are co-founders of Iconeus, which commercializes ultrasonic neuroimaging scanners.

Received: July 18, 2022
Revised: January 11, 2023
Accepted: March 22, 2023
Published: April 11, 2023

REFERENCES

1. Bolan, P.J., Yacoub, E., Garwood, M., Ugurbil, K., and Harel, N. (2006). In vivo micro-MRI of intracortical neurovasculature. Neuroimage *32*, 62–69. https://doi.org/10.1016/j.neuroimage.2006.03.027.
2. Lin, J., Weber, N., Wirth, A., Chew, S.H., Escher, M., Merkel, M., Kling, M.F., Stockman, M.I., Krausz, F., and Kleineberg, U. (2009). Time of flight-photoemission electron microscope for ultrahigh spatiotemporal probing of nanoplasmonic optical fields. J. Phys. Condens. Matter *21*, 314005. https://doi.org/10.1088/0953-8984/21/31/314005.
3. Ronzano, R., Roux, T., Thetiot, M., Aigrot, M.S., Richard, L., Lejeune, F.X., Mazuir, E., Vallat, J.M., Lubetzki, C., and Desmazières, A. (2021). Microglia-neuron interaction at nodes of Ranvier depends on neuronal activity through potassium release and contributes to remyelination. Nat. Commun. *12*, 5219. https://doi.org/10.1038/s41467-021-25486-7.
4. Williamson, M.R., Fuertes, C.J.A., Dunn, A.K., Drew, M.R., and Jones, T.A. (2021). Reactive astrocytes facilitate vascular repair and remodeling after stroke. Cell Rep. *35*, 109048. https://doi.org/10.1016/j.celrep.2021.109048.
5. Markicevic, M., Savvateev, I., Grimm, C., and Zerbi, V. (2021). Emerging imaging methods to study whole-brain function in rodent models. Transl. Psychiatry *11*, 457. https://doi.org/10.1038/s41398-021-01575-5.
6. Buzsáki, G., Anastassiou, C.A., and Koch, C. (2012). The origin of extracellular fields and currents — EEG, ECoG, LFP and spikes. Nat. Rev. Neurosci. *13*, 407–420. https://doi.org/10.1038/nrn3241.
7. Gupta, P., Balasubramaniam, N., Chang, H.-Y., Tseng, F.-G., and Santra, T.S. (2020). A single-neuron: current trends and future prospects. Cells *9*, E1528. https://doi.org/10.3390/cells9061528.
8. Logothetis, N.K., Pauls, J., Augath, M., Trinath, T., and Oeltermann, A. (2001). Neurophysiological investigation of the basis of the fMRI signal. Nature *412*, 150–157. https://doi.org/10.1038/35084005.
9. Niessing, J., Ebisch, B., Schmidt, K.E., Niessing, M., Singer, W., and Galuske, R.A.W. (2005). Hemodynamic signals correlate tightly with synchronized gamma oscillations. Science *309*, 948–951. https://doi.org/10.1126/science.1110948.
10. Viswanathan, A., and Freeman, R.D. (2007). Neurometabolic coupling in cerebral cortex reflects synaptic more than spiking activity. Nat. Neurosci. *10*, 1308–1312. https://doi.org/10.1038/nn1977.
11. Maier, A., Wilke, M., Aura, C., Zhu, C., Ye, F.Q., and Leopold, D.A. (2008). Divergence of fMRI and neural signals in V1 during perceptual suppression in the awake monkey. Nat. Neurosci. *11*, 1193–1200. https://doi.org/10.1038/nn.2173.
12. Bartolo, M.J., Gieselmann, M.A., Vuksanovic, V., Hunter, D., Sun, L., Chen, X., Delicato, L.S., and Thiele, A. (2011). Stimulus-induced dissociation of neuronal firing rates and local field potential gamma power and its relationship to the resonance blood oxygen level-dependent signal in macaque primary visual cortex. Eur. J. Neurosci. *34*, 1857–1870. https://doi.org/10.1111/j.1460-9568.2011.07877.x.
13. Nir, Y., Dinstein, I., Malach, R., and Heeger, D.J. (2008). BOLD and spiking activity. Nat. Neurosci. *11*, 523–524. https://doi.org/10.1038/nn0508-523.
14. Rees, G., Friston, K., and Koch, C. (2000). A direct quantitative relationship between the functional properties of human and macaque V5. Nat. Neurosci. *3*, 716–723. https://doi.org/10.1038/76673.
15. Lima, B., Cardoso, M.M.B., Sirotin, Y.B., and Das, A. (2014). Stimulus-related neuroimaging in task-engaged subjects is best predicted by concurrent spiking. J. Neurosci. *34*, 13878–13891. https://doi.org/10.1523/JNEUROSCI.1595-14.2014.
16. Mukamel, R., Gelbard, H., Arieli, A., Hasson, U., Fried, I., and Malach, R. (2005). Coupling between neuronal firing, field potentials, and fMRI in human auditory cortex. Science *309*, 951–954. https://doi.org/10.1126/science.1110913.
17. Klink, P.C., Aubry, J.-F., Ferrera, V.P., Fox, A.S., Froudist-Walsh, S., Jarraya, B., Konofagou, E., Krauzlis, R., Messinger, A., Mitchell, A.S., et al. (2021). Combining brain perturbation and neuroimaging in non-human primates. Neuroimage, 118017. https://doi.org/10.1016/j.neuroimage.2021.118017.
18. Das, A., Murphy, K., and Drew, P.J. (2021). Rude mechanicals in brain haemodynamics: non-neural actors that influence blood flow. Philos. Trans. R. Soc. Lond. B Biol. Sci. *376*, 20190635. https://doi.org/10.1098/rstb.2019.0635.
19. Lee, J.H., Durand, R., Gradinaru, V., Zhang, F., Goshen, I., Kim, D.-S., Fenno, L.E., Ramakrishnan, C., and Deisseroth, K. (2010). Global and local fMRI signals driven by neurons defined optogenetically by type and wiring. Nature *465*, 788–792. https://doi.org/10.1038/nature09108.
20. Kahn, I., Knoblich, U., Desai, M., Bernstein, J., Graybiel, A.M., Boyden, E.S., Buckner, R.L., and Moore, C.I. (2013). Optogenetic drive of neocortical pyramidal neurons generates fMRI signals that are correlated with spiking activity. Brain Res. *1511*, 33–45. https://doi.org/10.1016/j.brainres.2013.03.011.

21. Macé, E., Montaldo, G., Cohen, I., Baulac, M., Fink, M., and Tanter, M. (2011). Functional ultrasound imaging of the brain. Nat. Methods *8*, 662–664. https://doi.org/10.1038/nmeth.1641.

22. Bercoff, J., Montaldo, G., Loupas, T., Savery, D., Mézière, F., Fink, M., and Tanter, M. (2011). Ultrafast compound Doppler imaging: providing full blood flow characterization. IEEE Trans. Ultrason. Ferroelectr. Freq. Control *58*, 134–147. https://doi.org/10.1109/TUFFC.2011.1780.

23. Demené, C., Deffieux, T., Pernot, M., Osmanski, B.-F., Biran, V., Gennisson, J.-L., Sieu, L.-A., Bergel, A., Franqui, S., Correas, J.-M., et al. (2015). Spatiotemporal clutter filtering of ultrafast ultrasound data highly increases Doppler and fUltrasound sensitivity. IEEE Trans. Med. Imaging *34*, 2271–2285. https://doi.org/10.1109/TMI.2015.2428634.

24. Brunner, C., Grillet, M., Sans-Dublanc, A., Farrow, K., Lambert, T., Macé, E., Montaldo, G., and Urban, A. (2020). A platform for brain-wide volumetric functional ultrasound imaging and analysis of circuit dynamics in awake mice. Neuron *108*, 861–875.e7. https://doi.org/10.1016/j.neuron.2020.09.020.

25. Gesnik, M., Blaize, K., Deffieux, T., Gennisson, J.-L., Sahel, J.-A., Fink, M., Picaud, S., and Tanter, M. (2017). 3D functional ultrasound imaging of the cerebral visual system in rodents. Neuroimage *149*, 267–274. https://doi.org/10.1016/j.neuroimage.2017.01.071.

26. Aydin, A.-K., Haselden, W.D., Goulam Houssen, Y., Pouzat, C., Rungta, R.L., Demené, C., Tanter, M., Drew, P.J., Charpak, S., and Boido, D. (2020). Transfer functions linking neural calcium to single voxel functional ultrasound signal. Nat. Commun. *11*, 2954. https://doi.org/10.1038/s41467-020-16774-9.

27. Macé, É., Montaldo, G., Trenholm, S., Cowan, C., Brignall, A., Urban, A., and Roska, B. (2018). Whole-brain functional ultrasound imaging reveals brain modules for visuomotor integration. Neuron *100*, 1241–1251.e7. https://doi.org/10.1016/j.neuron.2018.11.031.

28. Boido, D., Rungta, R.L., Osmanski, B.-F., Roche, M., Tsurugizawa, T., Le Bihan, D., Ciobanu, L., and Charpak, S. (2019). Mesoscopic and microscopic imaging of sensory responses in the same animal. Nat. Commun. *10*, 1110. https://doi.org/10.1038/s41467-019-09082-4.

29. Bergel, A., Deffieux, T., Demené, C., Tanter, M., and Cohen, I. (2018). Local hippocampal fast gamma rhythms precede brain-wide hyperemic patterns during spontaneous rodent REM sleep. Nat. Commun. *9*, 5364. https://doi.org/10.1038/s41467-018-07752-3.

30. Dizeux, A., Gesnik, M., Ahnine, H., Blaize, K., Arcizet, F., Picaud, S., Sahel, J.-A., Deffieux, T., Pouget, P., and Tanter, M. (2019). Functional ultrasound imaging of the brain reveals propagation of task-related brain activity in behaving primates. Nat. Commun. *10*, 1400. https://doi.org/10.1038/s41467-019-09349-w.

31. Blaize, K., Arcizet, F., Gesnik, M., Ahnine, H., Ferrari, U., Deffieux, T., Pouget, P., Chavane, F., Fink, M., Sahel, J.-A., et al. (2020). Functional ultrasound imaging of deep visual cortex in awake nonhuman primates. Proc. Natl. Acad. Sci. USA *117*, 14453–14463. https://doi.org/10.1073/pnas.1916787117.

32. Norman, S.L., Maresca, D., Christopoulos, V.N., Griggs, W.S., Demene, C., Tanter, M., Shapiro, M.G., and Andersen, R.A. (2021). Single-trial decoding of movement intentions using functional ultrasound neuroimaging. Neuron *109*, 1554–1566.e4. https://doi.org/10.1016/j.neuron.2021.03.003.

33. Imbault, M., Chauvet, D., Gennisson, J.-L., Capelle, L., and Tanter, M. (2017). Intraoperative functional ultrasound imaging of human brain activity. Sci. Rep. *7*, 7304. https://doi.org/10.1038/s41598-017-06474-8.

34. Demene, C., Baranger, J., Bernal, M., Delanoe, C., Auvin, S., Biran, V., Alison, M., Mairesse, J., Harribaud, E., Pernot, M., et al. (2017). Functional ultrasound imaging of brain activity in human newborns. Sci. Transl. Med. *9*, eaah6756. https://doi.org/10.1126/scitranslmed.aah6756.

35. Demené, C., Mairesse, J., Baranger, J., Tanter, M., and Baud, O. (2019). Ultrafast Doppler for neonatal brain imaging. Neuroimage *185*, 851–856. https://doi.org/10.1016/j.neuroimage.2018.04.016.

36. Demené, C., Robin, J., Dizeux, A., Heiles, B., Pernot, M., Tanter, M., and Perren, F. (2021). Transcranial ultrafast ultrasound localization microscopy of brain vasculature in patients. Nat. Biomed. Eng. *5*, 219–228. https://doi.org/10.1038/s41551-021-00697-x.

37. Sans-Dublanc, A., Chrzanowska, A., Reinhard, K., Lemmon, D., Nuttin, B., Lambert, T., Montaldo, G., Urban, A., and Farrow, K. (2021). Optogenetic fUSI for brain-wide mapping of neural activity mediating collicular-dependent behaviors. Neuron *109*, 1888–1905.e10. https://doi.org/10.1016/j.neuron.2021.04.008.

38. Provansal, M., Labernède, G., Joffrois, C., Rizkallah, A., Goulet, R., Valet, M., Deschamps, W., Ferrari, U., Chaffiol, A., Dalkara, D., et al. (2021). Functional ultrasound imaging of the spreading activity following optogenetic stimulation of the rat visual cortex. Sci. Rep. *11*, 12603. https://doi.org/10.1038/s41598-021-91972-z.

39. Nunez-Elizalde, A.O., Krumin, M., Reddy, C.B., Montaldo, G., Urban, A., Harris, K.D., and Carandini, M. (2022). Neural correlates of blood flow measured by ultrasound. Neuron *110*, 1631–1640.e4. https://doi.org/10.1016/j.neuron.2022.02.012.

40. Musso, F., Brinkmeyer, J., Mobascher, A., Warbrick, T., and Winterer, G. (2010). Spontaneous brain activity and EEG microstates. A novel EEG/fMRI analysis approach to explore resting-state networks. Neuroimage *52*, 1149–1161. https://doi.org/10.1016/j.neuroimage.2010.01.093.

41. Huang, X., Long, Z., and Lei, X. (2019). Electrophysiological signatures of the resting-state fMRI global signal: a simultaneous EEG-fMRI study. J. Neurosci. Methods *311*, 351–359. https://doi.org/10.1016/j.jneumeth.2018.09.017.

42. Claron, J., Royo, J., Arcizet, F., Deffieux, T., Tanter, M., and Pouget, P. (2022). Covariations between pupil diameter and supplementary eye field activity suggest a role in cognitive effort implementation. PLoS Biol. *20*, e3001654. https://doi.org/10.1371/journal.pbio.3001654.

43. Cardoso, M.M.B., Sirotin, Y.B., Lima, B., Glushenkova, E., and Das, A. (2012). The neuroimaging signal is a linear sum of neurally distinct stimulus- and task-related components. Nat. Neurosci. *15*, 1298–1306. https://doi.org/10.1038/nn.3170.

44. Pisauro, M.A., Benucci, A., and Carandini, M. (2016). Local and global contributions to hemodynamic activity in mouse cortex. J. Neurophysiol. *115*, 2931–2936.

45. Mocanu, V.M., and Shmuel, A. (2021). Optical imaging-based guidance of viral microinjections and insertion of a laminar electrophysiology probe into a predetermined barrel in mouse area S1BF. Front. Neural Circuits *15*, 541676. https://doi.org/10.3389/fncir.2021.541676.

46. Sieu, L.-A., Bergel, A., Tiran, E., Deffieux, T., Pernot, M., Gennisson, J.-L., Tanter, M., and Cohen, I. (2015). EEG and functional ultrasound imaging in mobile rats. Nat. Methods *12*, 831–834. https://doi.org/10.1038/nmeth.3506.

47. Bergel, A., Tiran, E., Deffieux, T., Demené, C., Tanter, M., and Cohen, I. (2020). Adaptive modulation of brain hemodynamics across stereotyped running episodes. Nat. Commun. *11*, 6193. https://doi.org/10.1038/s41467-020-19948-7.

48. Claron, J., Hingot, V., Rivals, I., Rahal, L., Couture, O., Deffieux, T., Tanter, M., and Pezet, S. (2021). Large-scale functional ultrasound imaging of the spinal cord reveals in-depth spatiotemporal responses of spinal nociceptive circuits in both normal and inflammatory states. Pain *162*, 1047–1059. https://doi.org/10.1097/j.pain.0000000000002078.

49. Takata, N., Sugiura, Y., Yoshida, K., Koizumi, M., Hiroshi, N., Honda, K., Yano, R., Komaki, Y., Matsui, K., Suematsu, M., et al. (2018). Optogenetic astrocyte activation evokes BOLD fMRI response with oxygen consumption without neuronal activity modulation. Glia *66*, 2013–2023. https://doi.org/10.1002/glia.23454.

50. Saad, Z.S., Ropella, K.M., Cox, R.W., and DeYoe, E.A. (2001). Analysis and use of FMRI response delays. Hum. Brain Mapp. *13*, 74–93. https://doi.org/10.1002/hbm.1026.

51. Bandettini, P.A. (2014). Neuronal or hemodynamic? Grappling with the functional MRI signal. Brain Connect. *4*, 487–498. https://doi.org/10.1089/brain.2014.0288.

52. Boynton, G.M. (2011). Spikes, BOLD, attention, and awareness: a comparison of electrophysiological and fMRI signals in V1. J. Vis. *11*, 12. https://doi.org/10.1167/11.5.12.

53. Smith, S.M., Beckmann, C.F., Andersson, J., Auerbach, E.J., Bijsterbosch, J., Douaud, G., Duff, E., Feinberg, D.A., Griffanti, L., Harms, M.P., et al. (2013). Resting-state fMRI in the human connectome project. Neuroimage *80*, 144–168. https://doi.org/10.1016/j.neuroimage.2013.05.039.

54. Brookes, M.J., Woolrich, M., Luckhoo, H., Price, D., Hale, J.R., Stephenson, M.C., Barnes, G.R., Smith, S.M., and Morris, P.G. (2011). Investigating the electrophysiological basis of resting state networks using magnetoencephalography. Proc. Natl. Acad. Sci. USA *108*, 16783–16788. https://doi.org/10.1073/pnas.1112685108.

55. Yuan, H., Zotev, V., Phillips, R., Drevets, W.C., and Bodurka, J. (2012). Spatiotemporal dynamics of the brain at rest–exploring EEG microstates as electrophysiological signatures of BOLD resting state networks. Neuroimage *60*, 2062–2072. https://doi.org/10.1016/j.neuroimage.2012.02.031.

56. Britz, J., Van De Ville, D., and Michel, C.M. (2010). BOLD correlates of EEG topography reveal rapid resting-state network dynamics. Neuroimage *52*, 1162–1170. https://doi.org/10.1016/j.neuroimage.2010.02.052.

57. Ma, Y., Shaik, M.A., Kozberg, M.G., Kim, S.H., Portes, J.P., Timerman, D., and Hillman, E.M.C. (2016). Resting-state hemodynamics are spatiotemporally coupled to synchronized and symmetric neural activity in excitatory neurons. Proc. Natl. Acad. Sci. USA *113*, E8463–E8471. https://doi.org/10.1073/pnas.1525369113.

58. Ito, T., Brincat, S.L., Siegel, M., Mill, R.D., He, B.J., Miller, E.K., Rotstein, H.G., and Cole, M.W. (2020). Task-evoked activity quenches neural correlations and variability across cortical areas. PLoS Comput. Biol. *16*, e1007983. https://doi.org/10.1371/journal.pcbi.1007983.

59. Rabut, C., Correia, M., Finel, V., Pezet, S., Pernot, M., Deffieux, T., and Tanter, M. (2019). 4D functional ultrasound imaging of whole-brain activity in rodents. Nat. Methods *16*, 994–997. https://doi.org/10.1038/s41592-019-0572-y.

60. Sauvage, J., Poree, J., Rabut, C., Ferin, G., Flesch, M., Rosinski, B., Nguyen-Dinh, A., Tanter, M., Pernot, M., and Deffieux, T. (2020). 4D functional imaging of the rat brain using a large aperture row-column array. IEEE Trans. Med. Imaging *39*, 1884–1893. https://doi.org/10.1109/TMI.2019.2959833.

61. Baranger, J., Arnal, B., Perren, F., Baud, O., Tanter, M., and Demene, C. (2018). Adaptive spatiotemporal SVD clutter filtering for ultrafast Doppler imaging using similarity of spatial singular vectors. IEEE Trans. Med. Imaging *37*, 1574–1586. https://doi.org/10.1109/TMI.2018.2789499.

STAR★METHODS

KEY RESOURCES TABLE

REAGENT or RESOURCE	SOURCE	IDENTIFIER
Experimental models: Organisms/strains		
Rhesus non-human primate (Macaca mulatta)	Bioprim	N/A
Software and algorithms		
EventIDE	Okazolab, Netherlands	https://www.okazolab.com/
Plexon	Plexon Ins., TX, USA	https://plexon.com/
Plexon Offline Sorter	Plexon Inc., TX, USA	https://plexon.com/
MATLAB	The MathWorks In., MA, USA	https://www.mathworks.com/
Other		
Microelectrodes	Alpha Omega, USA FHC Inc., ME, USA	N/A
Functional ultrasound scanner prototype	Iconeus and Inserm U1273, Paris, France	N/A

RESOURCE AVAILABILITY

Lead contact

Further information and requests for resources should be directed to and will be fulfilled by the lead contact, Pierre Pouget (pierre.pouget@icm-institute.org).

Materials availability

This study did not generate new unique reagents.

Data and code availability

fUS imaging and electrophysiological data have been deposited at https://osf.io/v9xgb/and are publicly available as of the date of publication. Accession numbers are listed in the key resources table.

All original code has been deposited on the following link: https://osf.io/v9xgb/and is publicly available as of the date of publication.

Any additional information required to reanalyze the data reported in this paper is available from the lead contact upon request.

EXPERIMENTAL MODEL AND SUBJECT DETAILS

All experiments were ethically approved by the French "Ministère de l'Education, de l'Enseignement Supérieur et de la Recherche" under the project references APAFIS #6355–2016080911065046 and #9013–2017021515254591. Functional data were acquired from two captive-born rhesus monkeys (Macaca mulatta), S (male, 21 years old) and L (female, 15 years old), each one trained to perform different visual tasks.

METHOD DETAILS

Behavioral training

Monkeys were seated in a primate chair (Crist Instruments) with their head fixed and placed in front of a cathodic computer screen, 58cm away in a darkened booth. Mean screen luminance was controlled (1.15 mW cm^{-2}). Eye position of the primate was monitored at 1 kHz using an infrared video eye tracker (Eyelink 1k, SR-Research), which enabled live control of the behavioral paradigm and the delivery of a reward (sugary water) based on the success or failure of a visual task. Experiments were controlled by EventIDE software (Okazolab, Netherlands). Primates were under mild fluid restriction (approximately 30 mL/kg/day) and could drink ad libitum while working.

Behavioral paradigm for SEF data

Monkey S was trained to perform an active oculomotor task consisting of successive and randomized pro-saccades and antisaccades. After a baseline (100–120 s, random), the monkey had to perform a pro-saccade (look at the presented target) if the presented cue was a vertical rectangle or an anti-saccade (look on the opposite side of the presented target) if the above-mentioned rectangle was horizontal. After a successful trial, the monkey received a sugary water reward (few drops) and an intertrial of 3–4 s (time between

the end of a trial and the beginning of the next trial) was applied. If the trial was wrong, no sugary water was delivered and the intertrial started. The monkey worked for approximately 1 h.

Behavioral paradigm for V1 data

Monkey L was trained to perform passive fixation tasks. All sessions (except two) began with a 100s-baseline during which no stimuli were presented. The animal started the trial by fixing a central green square subtending 0.2 degrees of visual angle (DVA) for a random duration between 500 and 1000 ms within a tolerance window of 1.5 DVA. A visual stimulus of the peripheral location was then presented for 1s. We used different types of stimuli among sessions that were all localized in the left visual field. For most sessions, a single stimulus was presented. First, we used hemi-concentric bands of 2 DVA width centered on the central fixation point, filled with sinusoidal gratings with a fixed temporal frequency (one cycle per degree). The eccentricity was locked to 6 DVA. Second, we used polar angle stimuli that were 15 DVA of angular width extending from 1.5 to 15 DVA filled with sinusoidal gratings with a fixed temporal frequency (one cycle per degree). Third, we used gratings with varying spatial frequencies (3, 6, 9, 15 cycles per degree) in a rectangle area that covered the bottom-left quarter of visual field (DVA: -8 to 0 in the X axis, -7 to 0 in the Y axis). Fourth, we used a local checkerboard of 4*4 DVA center at R = 6 DVA and theta = $-\frac{3}{4}\pi$ radians. The animal was rewarded by a small drop of liquid (sugary water) at the end of each correct fixation trial. We imposed an intertrial interval of 9 s to ensure that the CBV value came back to the initial value. We also used control trials with the same temporal organization but without any peripheral visual stimulus. All conditions were randomly interleaved.

Implant and probe for functional ultrasound imaging for awake Cooperative monkeys

The head of the monkey was fixed using a surgically implanted titanium head post (Crist Instrument, MD, USA). After behavioral training of the animals, a recording chamber (CILUX chamber, Crist Instrument, MD, USA) was implanted and a craniotomy (diameter 19 mm) was performed (for monkey S: mediolateral: +0mm, anteroposterior: +26mm; for monkey L: mediolateral: +7 mm, anteroposterior: -10 mm, dorsoventral: +38 mm). A custom ultrasonic probe (128 elements, 15 MHz, 100 × 100 μm^2 of spatial resolution) with sterile ultrasonic gel was used in the chamber. The acquired images had a pixel size of 100 × 100 μm and a slice thickness of 400 μm. We could image 12 mm along the cortical surface and up to 15 mm in depth.

Functional ultrasound (fUS) recordings

Changes in CBV were measured using a real time functional ultrasound scanner prototype (Iconeus and Inserm U1273, Paris, France) with a custom 15-MHz linear probe. Data were acquired by emitting continuous groups of 11 planar ultrasonic waves tilted at angles varying from -10° to 10°. Ultrasonic echoes were summed to create a single compound image acquired every 2 ms. Final Doppler images were sampled at 2.5Hz by averaging 200 compound ultrasonic images after spatiotemporal filtering based on the singular value decomposition of the ultrasonic images.

Eye movements and pupil recordings

Eye movements were recorded during the tasks using a video eye tracker (Eyelink 1k, SR-Research) connected to an analog-to-digital converter (Plexon Inc, TX, USA). All data were collected using Plexon software and analyzed using MATLAB (The MathWorks Inc.,Massachusetts, USA). Saccades were detected when the eye's horizontal velocity went over 30°/s.

Online microelectrode position monitoring

We slowly (5 μm.s-1) inserted a microelectrode through the cortex via the adapter tube while performing live fUS imaging of the region of interest. The microelectrode is not visible in ultrasonic images and its location in the imaged plane is obtained by estimating local motion thanks to the Singular Value Decomposition (SVD) of the ultrasonic raw data. Because the electrode moved slowly, we adjusted the SVD clutter filter from $\lambda = 30$ to $\lambda = 2$ to track the electrode movement accurately rather than blood flow. We determined the optimum value for the SVD clutter filter in NPH using the adaptive spatiotemporal SVD as described by Baranger et al.[61] and determined $\lambda = 30$ as the optimum SVD clutter filter for the discrimination between tissue motion and blood flow in NHP. However, as the electrode is moving slower than red blood cells in vessels, we changed the clutter filter to isolate the insertion motion signal from the electrode and experimentally determined $\lambda = 2$ as the optimal value for the SVD clutter filter for online electrode monitoring.

Definition and conduct of a recording session

In this manuscript, we name 'session' an experiment during which we performed fUS while the animal performed the task. We recorded a total of n = 18 sessions for Monkey S, and for Monkey L, n = 79 sessions. Electrophysiological recordings were performed simultaneously in all Monkey S sessions (n = 18) and n = 53 sessions for Monkey L. Among these simultaneous recording sessions, we recorded 11 neurons and 17 neurons displaying significant activity in Monkey S and L, respectively. In general, we performed one session per day. For sessions in which we recorded simultaneous FUS imaging and single unit activity, we began by inserting the single-channel electrode to look for some neuronal activities. Once a stable unit was correctly isolated, we ran the behavioral task and then recorded fUS and neuronal signals. As we drilled only one tilted tube in the adapter for inserting the electrode and guide tube, the axis of the electrode was the same throughout the sessions.

Extracellular electrophysiological recordings

Extracellular neuronal activity were recorded *in vivo* simultaneously with fUS recording, using tungsten microelectrodes of impedance ranging from 8 to 10 MΩ for monkey S (ref UEWLGASEFN1E, FHC Inc, ME, USA) or glass-coated tungsten electrodes of impedance ranging from 0.5 to 2.5 MΩ for monkey L (ref. 366-120615-00, Alpha Omega, USA). The microelectrode was inserted into a 60 to 70mm stainless steel tubing and the tip of the microelectrode was connected to an amplifier with a male gold-plated pin connector (Ref. #520200, A-M Systems, WA, USA). The extracellular signal was amplified and collected using Plexon software. Offline spike analysis was performed manually using Plexon Offline Sorter (Plexon Inc, TX, USA). The microelectrode motion into cortical layers was performed using a micro-descender. For Monkey L, significantly-responsive units were determined by performing a Wilcoxon paired test (sign rank) of the mean firing rate value between a baseline ([-0.5 0] s) and a response window ([0 0.5] s) across all trials. We selected the units that displayed a p value $<5.10^{-4}$.

Setup preparation

The bottom of the recording chamber was filled with sterile ultrasonic gel. The ultrasonic probe and microelectrode with steel guide tube were inserted into the designed co-recording device. Hereafter, the device was inserted into the recording chamber, until contact with the ultrasonic gel. Appropriate position of the device was verified by fUS live view acquisition.

fUS data processing

Doppler data were analyzed using a generalized linear model approach implemented in MATLAB. The stimulation pattern, consisting of a Dirac comb with all cues presentations, in the design matrix was convoluted with the fUS-determined hemodynamic response function and a *Z* score and p value map were obtained. The activation maps show the *Z* score of all pixels in the images with a p value <0.001 (T-tests followed by Benjamini-Hochberg procedure to decrease false discovery rate). We chose the region of interest (ROI) within the supplementary eye field based on the *Z* score map and Paxinos atlas for macaque brains and the signal was averaged to obtain a single temporal signal. The spatially averaged signal was then expressed as the relative increase in CBV (in percent) by subtracting the baseline CBV (calculated during the baseline at the beginning of an acquisition) followed by division of the difference by the baseline CBV. Same analysis was run for V1.

Retinotopic maps

For these acquisitions (n = 46), we used the same passive fixation task as described earlier. The visual stimuli were hemi-concentric bands of 2 DVA width centered on the central fixation point, filled with sinusoidal gratings with a fixed temporal frequency (one cycle per degree). We used seven eccentricities ranging from 2 DVA to 14 DVA. For each acquisition, we performed seven parallel GLM analyses in which we used as entry the timings of a single condition presentation. To generate the retinotopic map for one acquisition, we selected for each pixel the condition displaying the highest *Z* score from those previous GLM analyses. Finally, we averaged maps that were obtained on the same imaging plane.

Processing of electrophysiological signals

Electrophysiological data were spike-sorted both online and offline, using Plexon software (Plexon Offline Sorter v4.5.1, Plexon, Dallas, TX, USA) during and after data acquisition. After the spike sorting, spikes are realigned on different time events (time of the cue presentation, time of the saccade for monkey S. and time of the reward) to determine the nature of the recorded neuron and the spike density function (SDF). The spike-density function was produced by convolving the spike train from each trial with a function resembling a postsynaptic potential specified by τg, the time constant for the growth phase, and τd, the time constant for the decay phase as $R(t) = (1 - \exp(-t/\tau d)*\exp(-t/\tau d)$. Based on physiological data from excitatory synapses τg was set to 1 ms and τd to 20 ms/50ms for Monkey S and Monkey L, respectively (59). The magnitude of the visual response was determined for each cell as the maximum value of the spike-density function during the time interval between the onset and the end of visual response. For the statistical parametric mapping, we needed an input signal linked to the neural activity. Here, we simply convolved spikes trains with the haemodynamic response function determined for each animal for their respective studied brain region (SEF for Monkey S. and V1 for Monkey L.) sampled at 1kHz and downsampled this signal to fUS imaging rate (2.5 Hz) before applying the generalized linear model for the statistical parametric mapping algorithm.

Cross-correlation between signals

In order to calculate the cross-correlation between fUS signal and spikes density function, we down-sampled the SDF to fUS signal frequency (2.5Hz). Signals were then cut in non-overlapping 10 s windows and cross-correlations were calculated using MATLAB xcorr function with 'normalized' option (in order to normalize signals in such a way that auto-correlation at null lag is equal to 1). This analysis was conducted for responsive-units only. Same protocol was used to calculate fUS-fUS cross-correlation. Afterward, in order to have the cross-correlation between our signals through time, we took into account the delay for which the absolute value of correlation or anti-correlation between signals was maximal: +2 s (SEF) and +5.2 s (V1) for fUS-SDF and 0 s for fUS-fUS cross-correlation. As we wished to compare the cross-correlation during the baseline and the cross-correlation during the task, we used paired T test after verifications of data normality using the Shapiro-Wilk test.

Table summarizing the recordings.

	Monkey S	Monkey L
fUS recordings acquisitions	21	79
fUS + ePhys recordings acquisitions	18	53
Non-responsive neurons	2	11
Responsive neurons	9	17

QUANTIFICATION AND STATISTICAL ANALYSIS

The n number for each experiment and details of statistical analyses (i.e., appropriate tests and associated p values) are described in the figure legends or main text. Data are reported as mean ± SEM. Statistical analyses were performed using MATLAB. For Generalized Linear Model analyses (Figures 2C, 2D, 3C, and 3D), p values were obtained by T-tests followed by Benjamini-Hochberg correction. For scatterplots in Figure 3, we assessed the significant differences between volumes and median Z-scores through Student T test (Figure 3F) and two-sample T test (Figure 3H). For Figure 4, all significant differences were assessed by paired T-tests.